

# Power Capture and Power Take-Off Load of a Self-Balanced Dual-Flap Oscillating Surge Wave Energy Converter

Alaa Ahmed<sup>1</sup>,

*Department of Civil, Environmental and Ocean Engineering, Stevens Institute of Technology Hoboken, NJ 07030*

Jia Mi

*Department of Naval Architecture and Marine Engineering University of Michigan, Ann Arbor, MI 48109*

Jianuo Huang

*Department of Naval Architecture and Marine Engineering University of Michigan, Ann Arbor, MI 48109*

Raju Datla

*Department of Civil, Environmental and Ocean Engineering, Stevens Institute of Technology, Hoboken, NJ 07030*

Kevin Connington

*Department of Mechanical Engineering, Stevens Institute of Technology, Hoboken, NJ 07030*

Lei Zuo

*Department of Naval Architecture and Marine Engineering University of Michigan, Ann Arbor, MI 48109*

Muhammad R. Hajj

*Department of Civil, Environmental and Ocean Engineering, Stevens Institute of Technology, Hoboken, NJ 07030*

---

<sup>1</sup>Corresponding author, Email address: aabdull2@stevens.edu

# Power Capture and Power Take-Off Load of a Self-Balanced Dual-Flap Oscillating Surge Wave Energy Converter

Alaa Ahmed<sup>1</sup>,

*Department of Civil, Environmental and Ocean Engineering, Stevens Institute of Technology Hoboken, NJ 07030*

Jia Mi

*Department of Naval Architecture and Marine Engineering University of Michigan, Ann Arbor, MI 48109*

Jianuo Huang

*Department of Naval Architecture and Marine Engineering University of Michigan, Ann Arbor, MI 48109*

Raju Datla

*Department of Civil, Environmental and Ocean Engineering, Stevens Institute of Technology, Hoboken, NJ 07030*

Kevin Connington

*Department of Mechanical Engineering, Stevens Institute of Technology, Hoboken, NJ 07030*

Lei Zuo

*Department of Naval Architecture and Marine Engineering University of Michigan, Ann Arbor, MI 48109*

Muhammad R. Hajj

*Department of Civil, Environmental and Ocean Engineering, Stevens Institute of Technology, Hoboken, NJ 07030*

---

## Abstract

Wave energy converters are an important part of future renewable energy infrastructure. Predicting their power matrix, capture width ratio, and power take-off loads at a targeted site is required for performance assessment before deployment. Because their testing is very expensive, numerical modeling and simulations play a significant role in those assessments. Linear potential flow theory has limited accuracy under large amplitude wave forcing. More accurate predictions can be obtained by using higher-fidelity models, which are computationally expensive. We present a framework for multi-fidelity numerical simulations to determine the hydrodynamic response, wave capture capability, and power take-off load of a full-scale dual-flap oscillating surge wave energy converter. This design exploits out-of-phase motion by setting the distance between the flaps to half the wavelength of the most occurring wave. The simulations are validated using a 1:10 model experiments in a wave tank. Based on these validations, it was determined that Euler simulations provide an acceptable prediction with 90% reduction in computational time with only 11% error. Utilizing Euler simulations at full-scale, the results demonstrate that the annual electrical energy output is 1.79 GWh under regular wave conditions. One significant improvement over single-flap designs is the capture width ratio which exceeds unity.

**Keywords:** Wave energy, Wave tank tests, Multi-fidelity simulations, Power matrix, Capture width ratio, PTO loads

---

<sup>1</sup>Corresponding author, Email address: aabdull2@stevens.edu

---

## 1. Introduction

Wave energy is a promising high-density renewable energy resource that can effectively mitigate climate warming by reducing our reliance on fossil fuels for electricity. In addition to the potential of integrating power generated from wave energy into electricity grids, wave energy can be effective in meeting power needs of coastal and isolated communities and coastal and offshore industries. For example, wave-powered desalination and aquaculture would improve the energy, water, and food security [1] and enhance economic conditions of coastal communities. Wave energy converters located near to the point of consumption can be considered an attractive solution for isolated areas lacking electricity services, where the installation of power lines is not profitable [2]. Different mechanisms and designs for wave energy converters (WECs) have been proposed. Based on the wave capture structure, WECs can be classified as oscillating water columns (OWC) [3–6], overtopping devices [7–9], and wave-activated bodies [10–12]. The operation of wave-activated bodies is based on wave-induced oscillations of buoys or flaps that capture the hydrokinetic energy and convert it into useful energy using a power takeoff (PTO) mechanism [13]. One desirable feature of flap-type surge converters, referred to as oscillating surge wave energy converters (OSWECs) in the literature, is that they have a higher energy capture efficiency [10, 14, 15] than oscillating water columns or overtopping devices. The OSWEC is a single degree of freedom device, placed perpendicular to the wave propagation direction, hinged at one end, and rotates as the crest and trough pass by the free end. In shallow waters, the flap could be directly hinged to the seabed [16, 17]. Folley et al. [18] noted that positioning the device in deeper waters will result in larger captured power. To operate in deep water the flap would have to be hinged to a supporting platform that is held by mooring lines. One concept of an OSWEC to operate in deep water on a floating platform is the Reference Model 5 (RM5) [19]. Another concept of floating oscillating surge wave energy converter (FOSWEC) proposed by Pecher et al. [20], consists of a pair of pitching flaps each hinged to the supporting platform.

Determining a WEC performance at the full-scale can be based on different factors including its capability to absorb wave power and its cost. Full-scale testing of different concepts of WECs is very costly, especially in deep waters [21]. The variability of wave resources in different regions adds to the complexity of advancing towards a dominant concept or optimal WEC configuration. In order to assess a WEC performance, different approaches have been followed. Babarit et al. [22] used governing equations with assumed coefficients to estimate the power matrices of different devices. Various studies used wave data and rated power of different types of WECs to determine the power matrix and estimated the electrical power in different regions of the world [23–26]. Kelly et al. [27] investigated the effect of the geometry control of an OSWEC on annual power generation and computed the power matrices at three different U.S. wave energy sites. Ni and Peng [28] used a convolution neural network to predict the wave power absorbed by a pendulum WEC to estimate the power matrix. Rahimi et al. [29] used Budal’s theory to predict an upper bound for WEC power absorption and applied it on the absorbed power using wave data to assess the performance. Babarit [10] used the capture width ratio (CWR), defined as the ratio of absorbed wave power  $P$  (in kW) to the wave resource (in kW/m) over the width of the WEC as the basis for power performance. Majidi et al. [30] evaluated the power and production performance of fifteen

different full-scale WECs when deployed in the black sea using multiple parameters including: the capacity factor, capture width ratio, dimensionless normalized wave power, and efficiency index. Carballo et al. [31] tested three different WECs at different sites. Their results showed that the capacity factor and capture width ratio are the most significant parameters capable of characterizing detailed hydrodynamic performance. Astariz and Iglesias [32] used the levelized cost of electricity (LCOE), in \$/kWh, to assess the cost effectiveness of different WECs.

Numerical simulations provide a relatively inexpensive alternative to assess or optimize a specific design in terms of its efficiency, CWR, PTO loads and control strategies, mooring configuration, and capital and operational costs which are important before triggering real ocean tests. Numerical simulations can also be used to verify the WEC's capability to produce annual energy in the targeted sites and ability to survive extreme load conditions. These simulations can also be useful in assessing the hydrodynamic characteristics and optimizing the response of a specific WEC. Numerical simulations can have different fidelities based on the equations being solved. Low-fidelity models solve the potential flow, while high-fidelity models solve the Reynolds Averaged Navier-Stokes (RANS). Ruehl et al. [33] performed numerical simulations using the open-source WEC-Sim code on a 1:33-scale FOSWEC. These simulations were tuned using experimental data from tests on four configurations over a range of different conditions. The results demonstrated that, with some limitations, WEC-Sim is able to accurately simulate the response of the FOSWEC when subject to regular waves. They noted the need to incorporate nonlinear hydrodynamics into the WEC-Sim simulation to improve the simulation accuracy. Bhinder et al. [34] implemented a potential time domain viscous model to assess the importance of the viscous forces regarding OSWECs. They observed that adding a Morison drag term improves the predictions significantly. Lin et al. [35] validated the WEC-Sim predictions of the wave energy absorption by an OSWEC using predictions from RANS simulations of FLOW-3D, their results showed that viscous losses reduce the capture factor by 19% on the average. Wei et al. [36] used ANSYS FLUENT to simulate an OSWEC and validated the simulations with experimental data. They showed that the volume of fluid (VOF) method with the layering method in dynamic mesh can successfully simulate the wave loading. Schmitt and Elsaesser [37] determined that simulations performed using interDyMFOAM solver from the OpenFOAM toolbox efficiently predicted the motion of the flap. Bhinder et al. [38] performed experiments on a WRASPA (Wave-driven, Resonant, Arcuate action, Surging Point-Absorber) to validate the numerical simulations using Flow-3D, the numerical results showed a good agreement with the experimental data for the free decay tests. However, the simulations underestimated the pitch motion. In summary, low-fidelity simulations inadequately capture the non-linearities that significantly impact solution accuracy, particularly under high amplitudes. On the other hand, high-fidelity simulations, while computationally demanding, offer accurate results. Achieving a balance between computational efficiency and accuracy is essential for effective modeling of WECs, especially at full-scale.

The research effort presented in this paper is to assess the performance of a self-balanced full-scale dual-flap OSWEC for potential testing in the PacWave south test site with the proposition of exploiting out-of-phase oscillating surge flaps [20, 33, 39, 40]. The out-of-phase flap motions result in opposing wave forces and moments on the flaps and supporting platform yielding reduced platform motions, stresses on hinges and supporting elements, and reaction forces on mooring lines [41, 42]. The cumulative power from each flap yields a higher

level of energy generation in comparison to single flap systems mounted on separate supporting platforms. The major advantage of this design over single flap OSWEC is the increased CWR by two flaps mounted on a single platform for the purpose of reducing the levelized cost of electricity. Our approach is to use numerical simulations validated against WEC-specific experimental data as noted by Lawson et al. [43] to determine potential power output of the proposed design. Towards that objective, a 1:10-scale model is fabricated and tested in a wave tank. These tests are then used to validate numerical simulations having different levels of fidelity. Once validated, the numerical simulations are used to carry out more extensive simulations of the full-scale self-balanced OSWEC using PacWave south wave data. Initial validation showed that linear potential flow theory has limitations on accurate predictions of the hydrodynamic response, especially under large wave amplitude conditions. This highlights the importance of including nonlinearities in the solution to realistically predict the power output at full-scale, which comes in agreement with the findings in [44]. As such, the performed simulations are based on accuracy assessment of RANS and inviscid (Euler) simulations and different mesh resolutions in terms of output accuracy versus computational cost. Based on this assessment, the power matrix, CWR, and PTO loads are estimated for the full-scale OSWEC.

The major contributions of this study are (1) to present a framework for validated multi-fidelity simulations as an effective approach to assess the performance for a full-scale OSWEC; (2) to experimentally test the hydrodynamic response of a 1:10-scaled model of the proposed design; (3) to use these tests to validate multi-fidelity simulations and assess their accuracy vis-a-vis their computational cost; (4) to predict the power matrix, CWR, and PTO loads for the full-scale OSWEC at a targeted site, namely the PacWave South site. Given the challenges of varying wave resources in different parts of the world (e.g., differences of wave characteristics along the east and west coasts of the United States) and given the much needed innovations to reduce the LCOE costs, the presented framework, which is based on experimentally-validated multi-fidelity numerical simulations, provides the capability to consider many configurations at the conceptual design stage in the design process in contrast to running high-fidelity simulations that would not allow the consideration of a broad range of configurations because of their computational costs or to low-fidelity simulations based on unjustified assumptions or to low-fidelity simulations based on unjustified assumptions that may result in significant errors. Particularly, demonstrating the usability of this framework in assessing the performance of the proposed self-balanced full-scale dual-flap OSWEC allows for extending it in the future to designs having different separation between the two flaps or flaps' geometries. It also demonstrates its usability for developing efficient designs for different locations having different wave resources.

This paper is organized as follows. The wave resources at PacWave south and conceptual design of the self-balanced dual-flap OSWEC are detailed in Section 2. Section 3 summarizes the background for the multi-fidelity simulations. In section 4, the setup for the 1:10 scaled model experiments in a wave tank is detailed and validation of the different simulations is carried out. The power matrix, CWR, and PTO load estimates are presented in Section 5. The conclusions are drawn and summarized in Section 6.

## 2. Wave resources at PacWave South and WEC conceptual design

PacWave is an open ocean wave energy testing facility consisting of two (North and South) sites with the south site located at 44.557°N, 124.229°W, [45]. The mean water depth at the PacWave south location is 67.4 m. The joint probability distribution used for evaluating the performance of the proposed dual-flap OSWEC, which defines the percent of occurrence of a specified significant wave height and corresponding energy period is presented in Figure 1. The most commonly occurring seas with a significant wave height of 1.75 m and an energy period of 8.5 s occur for 578 hours per year, while the highest annualized wave energy sea state occurs for 331 hours per year at a significant wave height of 2.75 m and at an energy period of 10.5 s.

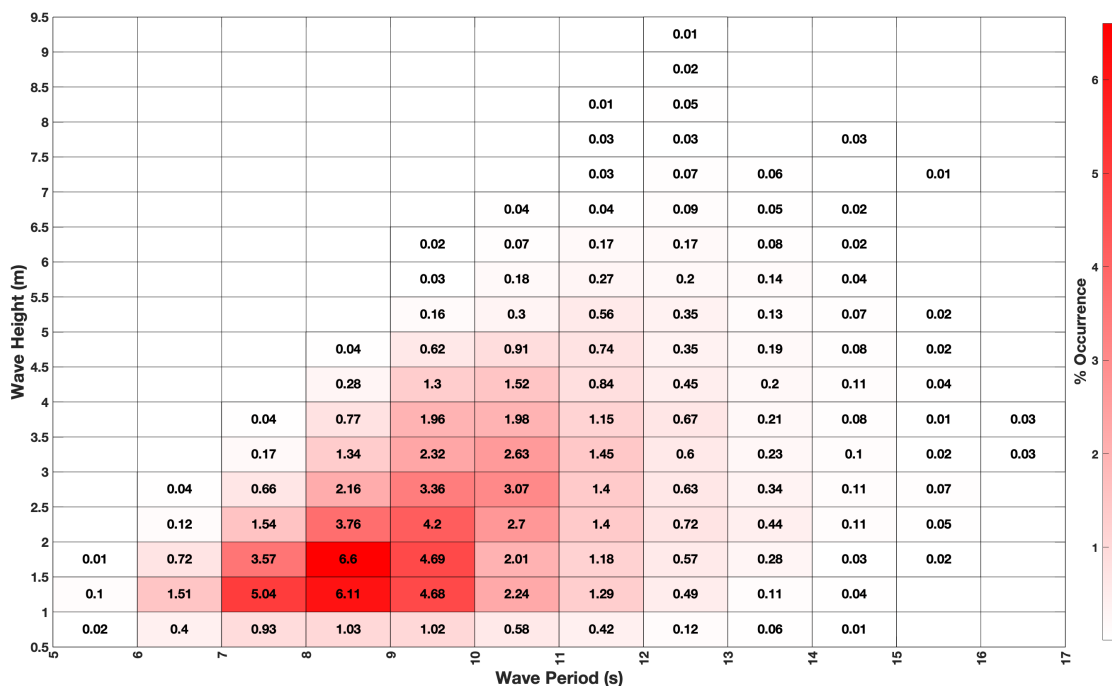


Figure 1: Joint probability distribution (JPD) of sea states for SETS - frequency of occurrence [39]

As stated above, the self-balanced dual-flap OSWEC under consideration consists of two pitching flaps mounted on a supporting platform as schematically shown in Figure 2. Each flap is hinged to a horizontal shaft. The two flaps are placed such that their planes are perpendicular to the incident wave. They are separated by half the wavelength (55 m) of the most occurring wave to exploit the out-of-phase motion. The power is generated from the relative pitch motion between the flap and platform. The geometric and mass properties of the full-scale, based on most occurring wave at the PacWave south, and 1:10 model scale of the self-balanced dual-flap OSWEC are presented in Table 1. Scaling between the tank experiments and the full scale was done based on Froude number [46].

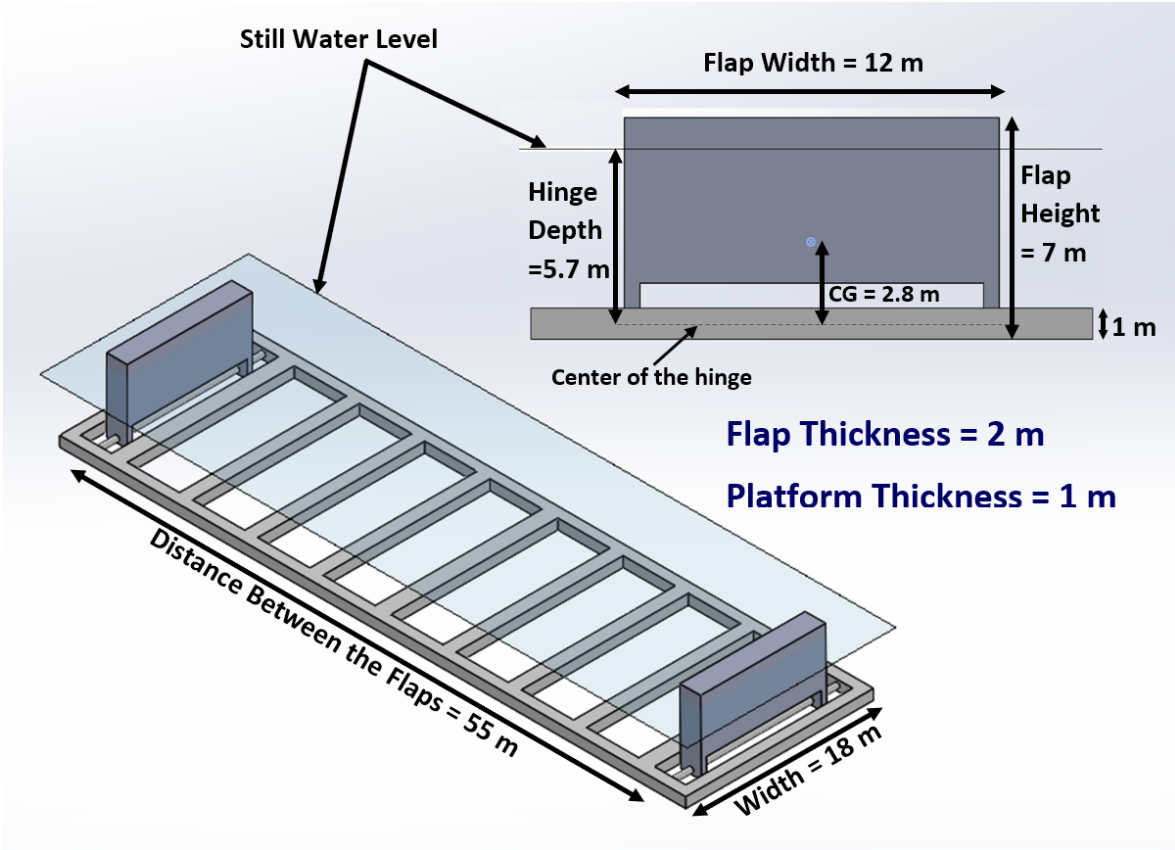


Figure 2: Schematic of full scale self-balanced dual-flap OSWEC

Table 1: Dimensions and mass properties of full-scale and scaled-model flap

Parameters	Full-scale	1:10 scaled model
Width x height x thickness	12x7x2 m	1.2 x 0.7 x 0.2 m
Mass	35 tons	35 kg
Mass moment of inertia	$10^3 \text{ ton} \cdot \text{m}^2$	$10 \text{ kg} \cdot \text{m}^2$
Hinge depth from still water level	5.7 m	0.57 m
Center of gravity (CG) location from hinge	2.8 m (40%)	0.28 m (40%)
Flap draft	6 m (86%)	0.6 m (86%)
Distance between the flaps (hinge to hinge)	55 m	4.88 m

### 3. Multi-Fidelity simulations

As aforementioned, numerical modeling plays a significant role in the performance assessment of WECs, especially at full-scale, due to the complexity and cost of their testing in open water. Although high-fidelity simulations can accurately predict the hydrodynamic response of the WEC, it is computationally expensive and inconvenient in the early stages of design. Furthermore, low-fidelity simulations can be fast, but overpredicts the response. A balance between the computation cost and accuracy can be presented by utilizing a medium-fidelity simulations when solving Euler’s equations. The multi-fidelity framework presented in Figure 3 illustrates our

approach to assess the performance of the full-scale OSWEC. This framework balances the computational need and expense with the accuracy of the hydrodynamic simulations based on model testing.

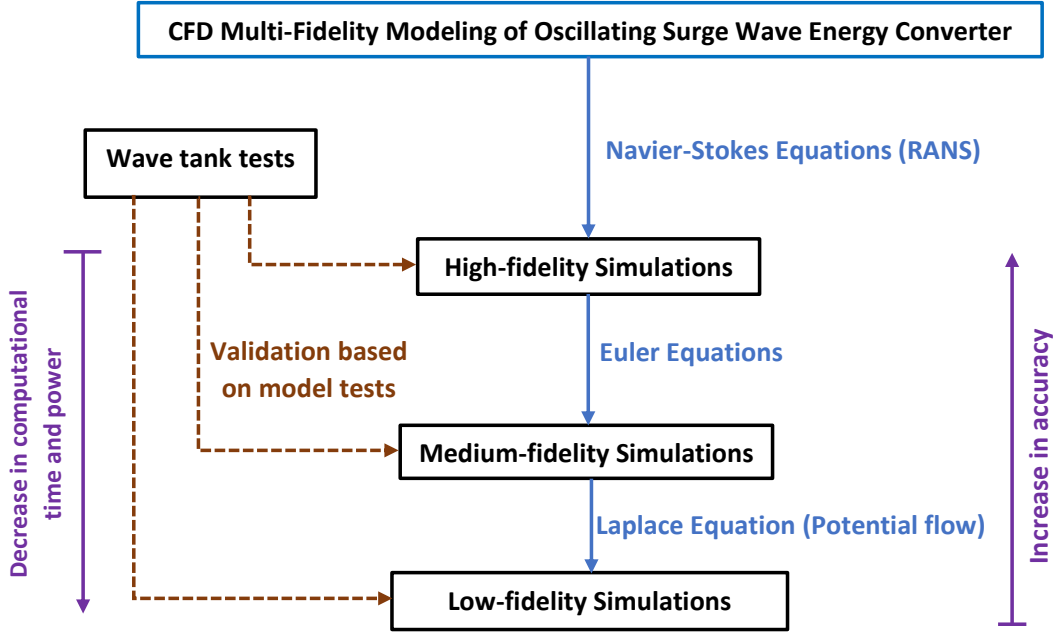


Figure 3: Framework for multi-fidelity simulations of the hydrodynamic response of the OSWEC

### 3.1. Governing equations

All numerical simulations were performed using the commercial computational fluid dynamics (CFD) software solvers ANSYS AQWA and ANSYS FLUENT. As implemented, AQWA assumes potential flow and solves the Laplace equation along with the unsteady Bernoulli equation to determine the forces and moments acting on the flaps. FLUENT solves the conservation equations for mass and momentum using the finite volume method. As a first step, we carried out potential flow and unsteady viscous and inviscid flow simulations at the model scale to determine their computational cost vis-a-vis their accuracy when compared with experimental data. In the viscous simulations, the Reynolds-averaged Navier–Stokes (RANS) equations, derived by taking the time average of the Navier–Stokes equations, and written as [47]

$$\frac{\partial U_i}{\partial x_i} = 0 \quad (1)$$

$$\frac{\partial U_i}{\partial t} + U_j \frac{\partial U_i}{\partial x_j} = -\frac{1}{\rho} \frac{\partial P}{\partial x_i} + \frac{\partial}{\partial x_j} \left( \nu \frac{\partial U_i}{\partial x_j} - \overline{u_i u_j} \right) + g_i \quad (2)$$

are solved. In these equations,  $u_i$  represents the velocity vector,  $U_i$  is the time-averaged velocity vector,  $\rho$  is the density,  $P$  is the time-averaged pressure,  $\nu$  is the kinematic viscosity, and  $g_i$  is the gravitational acceleration vector. Different RANS models can be employed as empirical closure hypotheses to compute the Reynolds stress tensor  $\overline{u_i u_j}$ . The most dependable closure models are the two-equation closures, which solve one additional

equation for the turbulent kinetic energy  $k$ , and another one for either the dissipation  $\epsilon$ , or the dissipation rate  $\omega$ . These are respectively referred to as the  $k$ - $\epsilon$  and  $k$ - $\omega$  models. The inviscid simulations are performed by solving the Euler equations [48]

$$\frac{\partial u_i}{\partial x_i} = 0 \quad (3)$$

$$\frac{\partial u_i}{\partial t} + u_j \frac{\partial u_i}{\partial x_j} = -\frac{1}{\rho} \frac{\partial p}{\partial x_i} + g_i \quad (4)$$

The free surface is modeled using the volume of fluid (VoF) method where a single set of equations are solved for the water and air using their volume fraction represented by  $\gamma$  that is tracked throughout the domain. The equations for each cell is written as [49]:

$$\frac{\partial \gamma}{\partial t} + u_i \frac{\partial \gamma}{\partial x_i} = 0 \quad (5)$$

The values of  $\gamma$  vary between 0 and 1 with a zero value indicating that the cell is empty of the water, while a one value indicates a cell that is full of water. Values of  $\gamma$  between zero and one indicate that the cell contains a free surface.

### 3.2. Numerical Domain

The computational domain reflected the geometry of the wave tank of the Davidson Laboratory, where the model tests were performed, except in the length where only a third of its length is simulated to reduce the computational cost. The domain's width is 5m, depth is 3m, and length is 35m. This domain was discretized into non-overlapping finite volumes in which the discretized governing equations were solved to obtain the velocity field, pressure, and volume of fraction of the flow. The domain was divided to three zones as shown in Figure 4. The left and right zones were discretized using a structured mesh (hexahedral cells) while the middle zone was discretized using unstructured mesh (tetrahedral cells). The flaps were set in the middle zone and a dynamic mesh was employed to describe their rotation. The middle zone was considered as a deforming zone that changed with time. Smoothing and re-meshing methods were used to keep the quality of the updated cells, whereas the left and right zones were stationary. As shown in Figure 4, the cell size was smallest around the flap, larger in the left zone, and largest in the right zone. To ensure a grid-independent solution, simulations were carried out subsequently by refining the grid through increasing the number of cells.

The computational domain of the simulations was subjected to the inlet (upstream), outlet (downstream), atmospheric, bottom, and flap surface boundary conditions. The upstream boundary condition is a velocity inlet, open channel wave boundary condition, which was activated to generate regular or irregular waves. The free surface boundary is set to be pressure outlet to simulate the air at atmospheric pressure (Figure 5). The side and bottom boundaries are set to be walls with no slip conditions. A numerical beach is simulated at the outlet boundary to damp the waves and prevent wave reflection. Initially, the flaps were set in their upright position without the presence of waves.

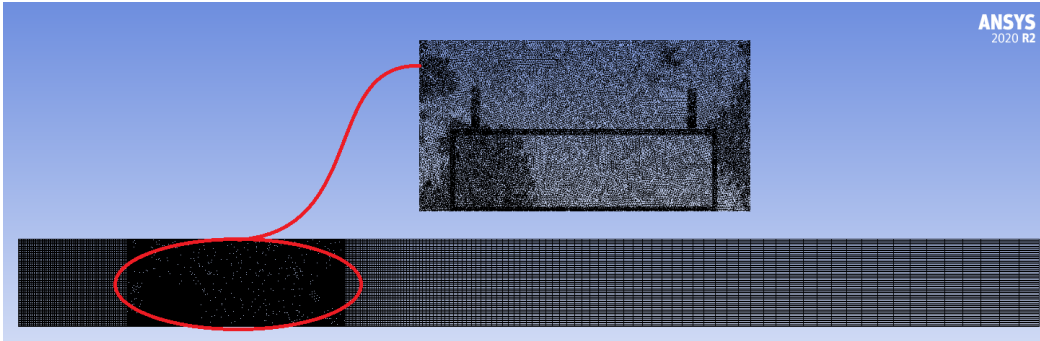


Figure 4: Zones and meshing of the computational domain for the 1:10 model in the wave tank

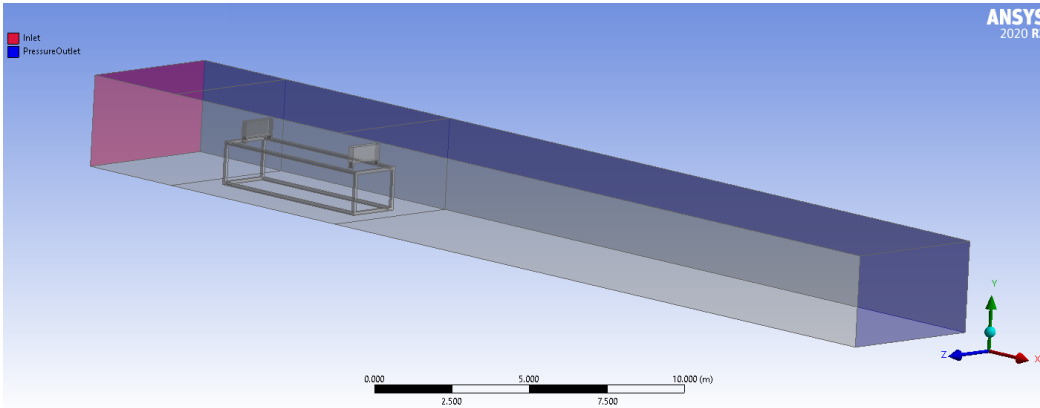


Figure 5: Boundary conditions of the computational domain for the 1:10 model in the wave tank

The governing equations were solved using the coupled pressure-based solver in ANSYS FLUENT. In this solver, the system of momentum and pressure-based continuity equations are solved simultaneously [50]. The Pressure-Implicit with Splitting of Operators (PISO), which is employed in simulations involving large time steps and high degree of mesh distortion [51], was chosen for pressure-velocity coupling. The body-force-weighted scheme was used for pressure discretization to include the body force in the calculations. The compressive scheme was used to obtain the face fluxes for all cells for the volume fraction equation. The second order upwind was selected for momentum discretization, and the first order upwind was selected for turbulence model. The solution was considered to converge when all the residuals are less than  $10^{-3}$  for all variables.

### 3.3. Wave generation

Waves are generated using the open channel wave boundary condition. It is an upstream boundary condition applied to the velocity inlet of the VoF model that allows to simulate the propagation of waves. One of the common issues in the numerical wave tank is the wave absorption, as the waves might reflect back into the domain. In order to stop or reduce that reflection, a numerical beach is modeled at the end of the numerical domain to damp the waves. Regular monochromatic waves were simulated based on a wave profile,  $\eta$  that is represented by [52]

$$\eta(x, t) = A \cos(kx - \omega t) \quad (6)$$

where  $A$  is the wave amplitude,  $k$  is the wavenumber, and  $\omega$  is the wave frequency.

The same inlet condition is applied to generate irregular waves as modeled using the Pierson-Moskowitz spectrum [52], which assumes that waves are in equilibrium with the wind over unlimited fetch. It is valid for fully developed sea and modeled by:

$$S_{PM}(\omega) = \frac{5}{16} \frac{H_s^2 \omega_p^4}{\omega^5} e^{\left(-\frac{5\omega^4}{4\omega_p^4}\right)} \quad (7)$$

where  $\omega$  is the wave frequency,  $\omega_p$  is the peak wave frequency, and  $H_s$  is the significant wave height.

### 3.4. Flap dynamics

The hydrodynamic torque acting on the pitching flap is computed by integrating the dynamic pressure over the flap surface. This torque,  $T$  includes contributions from the excitation torque from the waves, the radiation damping torque, and the torque due to buoyancy. The angular acceleration,  $\ddot{\theta}$ , is then calculated from the equation of motion derived by applying Newton's second law [53]:

$$I_{flap} \ddot{\theta} = T \quad (8)$$

where  $I_{flap}$  is the mass moment of inertia of the flap.

The angular velocity,  $\dot{\theta}$ , is derived by numerically integrating  $\ddot{\theta}$  using fourth-order multi-point Adams-Moulton formulation [54]:

$$\dot{\theta}^{n+1} = \dot{\theta}^n + \frac{\Delta t}{24} (9\ddot{\theta}^{n+1} + 19\ddot{\theta}^n - 5\ddot{\theta}^{n-1} + \ddot{\theta}^{n-2}) \quad (9)$$

This velocity is used to update the dynamic mesh with the new flap position.

### 3.5. Assessment of turbulence closure models

Turbulence closure models implemented in the RANS solver differ in accuracy and computational cost from one flow to another. The k- $\epsilon$  is the most extensively validated and used. To compare the cost and accuracy, we performed simulations under the same conditions using the standard k- $\epsilon$  (SKE), re-normalization group k- $\epsilon$  (RNG), realizable k- $\epsilon$  (RKE), standard k- $\omega$  (SKW), and shear stress transport k- $\omega$  (SST). A comparison of the generated flap rotations using these models is presented in Figure 6. The results show that all models predict the rotation to more or less to the same level of accuracy. Although the standard k- $\epsilon$  model has the lowest computational cost, the realizable k- $\epsilon$  is better suited when modelling flows around bluff bodies [55] that exhibit streamline curvature and vortex shedding as generated by the rotating flap. As such, the realizable k- $\epsilon$  model is used in all presented RANS simulations.

## 4. Tank test validation of numerical simulations

Series of experiments were performed in the wave tank of the Davidson Laboratory at Stevens Institute of Technology to validate the accuracy of the numerical simulations in determining the response of the flaps. As shown in Figure 7, the tank is 100m long, 5m wide and 3m deep. The water depth of 2m is constant. The waves are generated by a 6-paddle wave maker that can generate wave periods up to 5 sec and wave heights up to

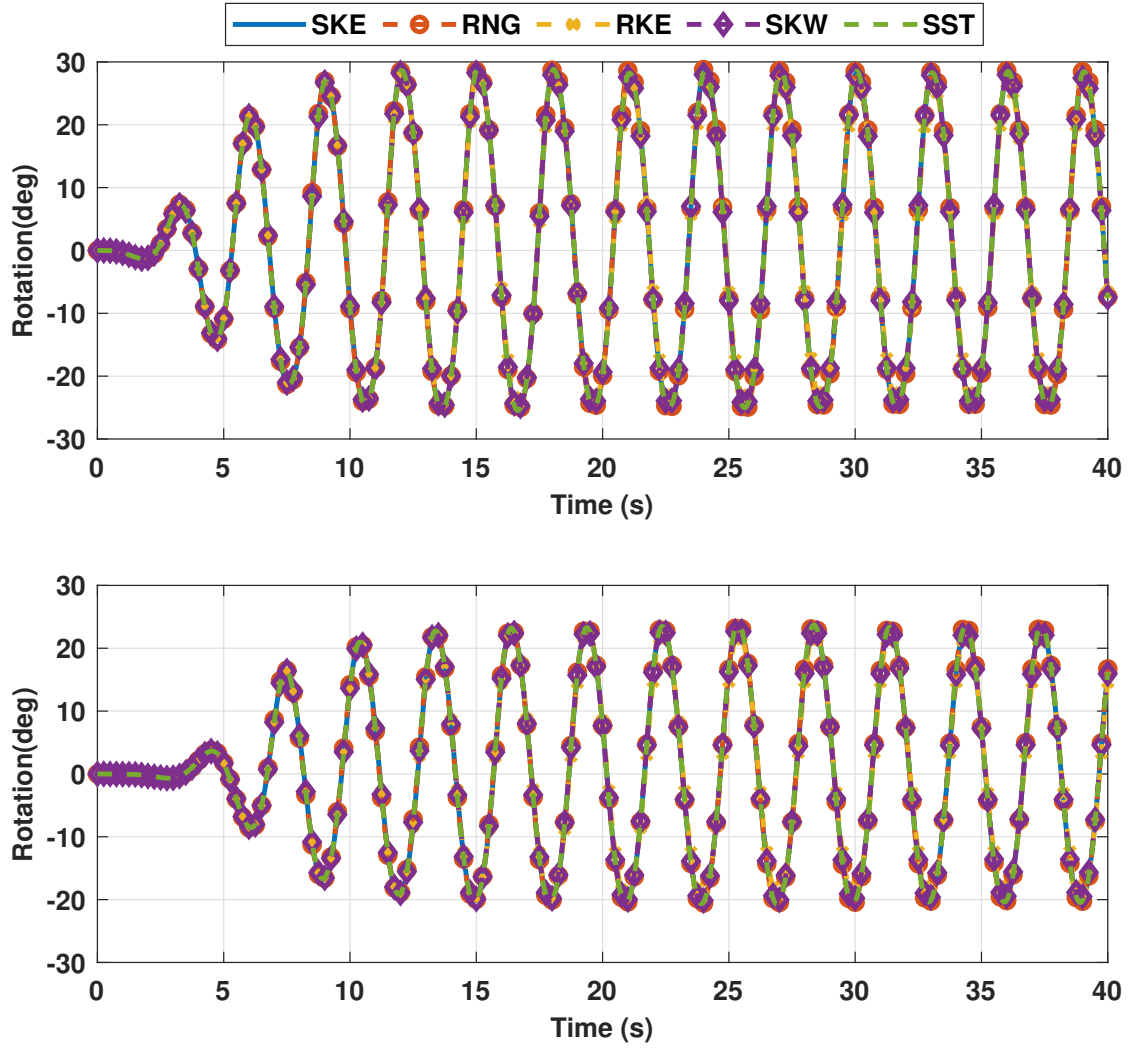


Figure 6: Comparison between different turbulence models under regular wave excitation for waves with a period of 3 seconds and a height 0.08m for front flap (top) and back flap (bottom)

0.65m as shown in Figure 8. All experiments were performed on a 1:10 scale model whose geometric and material properties are presented in Table 1. The flap is composed of a rectangular aluminum box filled with foam and a window opening at the bottom. The frame was hinged to a shaft mounted on a box-shaped base fixed to the tank floor. The base is 1.4m high, which resulted in the flaps piercing the free surface at an elevation of 0.6m draft. The window opening is 1.1m wide, 0.17m high, and 0.2m thick. The flaps, as pictured in Figure 9, were positioned in the middle of the tank. Two wave probes were located upstream and downstream of the flap to record the wave height data. The pitch angle of the flap was measured by a linear variable differential transformer (LVDT) sensor, and data was sampled at the rate of 100 Hz. The experimental data was used to validate the numerical simulations.

In this study, the validation is based on comparing numerical simulations and experimental measurements of free decay and forced flap responses of the model scale. Additional validation is based on comparing values of

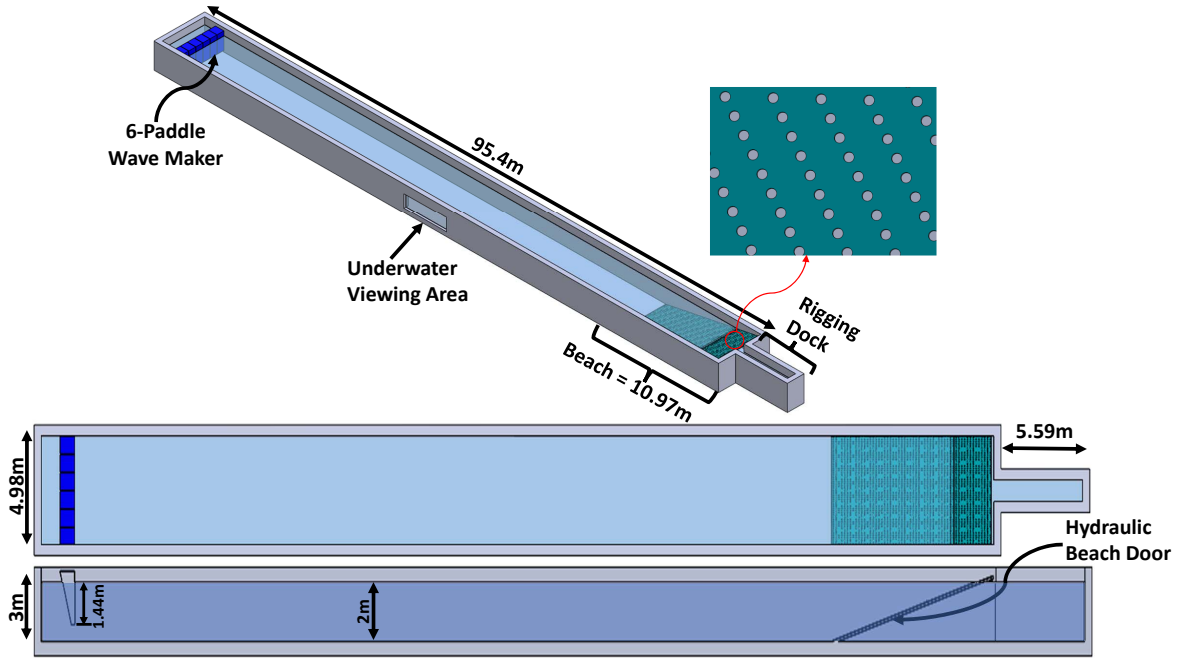


Figure 7: Schematic for the Davidson laboratory high speed towing tank

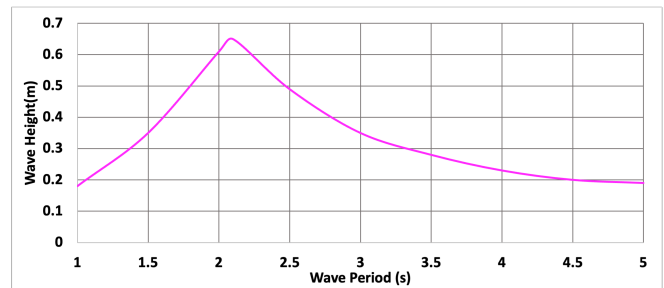
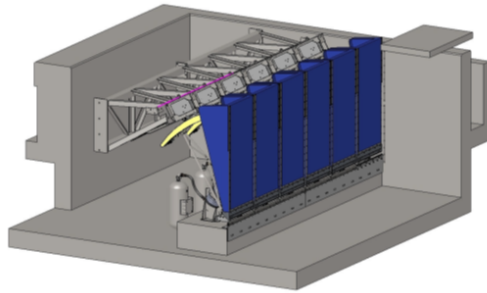


Figure 8: Illustration of Davidson lab flap wave maker and properties of generated waves

the natural frequency ( $\omega_n$ ), damping ratio ( $\zeta$ ), and added mass moment of inertia ( $I_{added}$ ) from the simulations and experiments. Figure 10 compares free decay plots of the two flaps obtained from RANS simulations against experimentally measured rotations. The plots show a high level of agreement especially during the first four cycles. The subsequent small discrepancies are most likely due to the difference in the lengths of the numerical domain and the wave tank. A comparison of the experimentally measured and simulated values of natural frequency, damping ratio, added mass moment of inertia, and radiation damping coefficient is presented in Table 2. It is noticed that there is a difference in damping between the two flaps in the experimental results. This difference

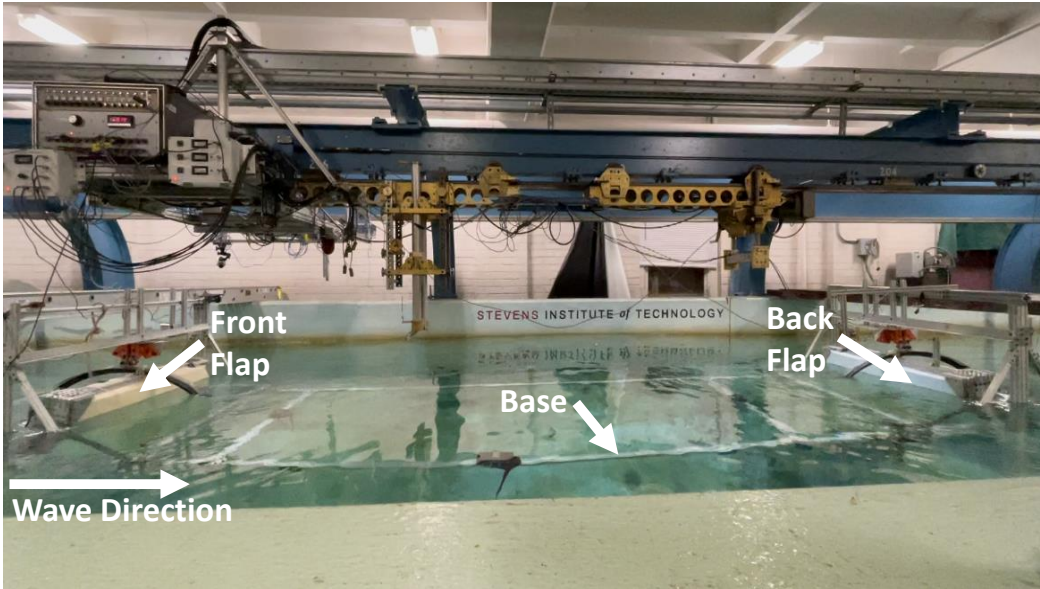


Figure 9: Picture of the 1:10 scaled dual-flap OSWEC model as set in the wave tank

is due to the higher friction of mechanical parts, which emphasizes the importance of quality control during manufacturing. To represent the additional friction of the back flap in the simulations, we added mechanical damping to its governing equation of motion. The errors in all determined values were less than 2% for the front flap and less than 4% for the back flap indicating a high level of agreement.

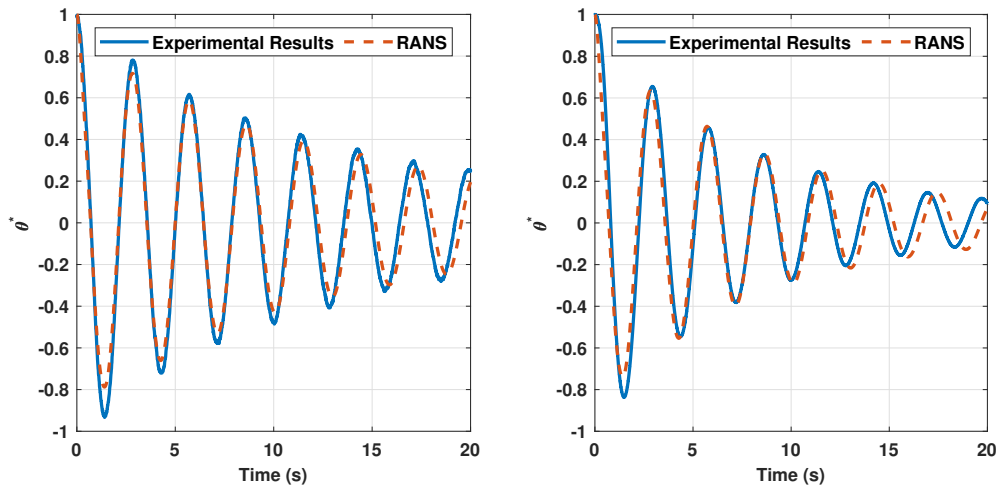


Figure 10: Comparison of time series from free decay tests and high-fidelity simulations with normalized initial displacement for front flap (left) and back flap with added mechanical damping in the numerical simulation (right)

Further validation is carried out by comparing amplitudes of flap rotation under regular wave forcing. A series of experiments and simulations covering different values of wave periods and amplitudes were performed. To assess the validity of assuming potential flow, we compare in Figure 11 the time series of the experimental measurements with the time series obtained by integrating the governing equation using hydrodynamic coefficients as determined by AQWA. The plots show a significant discrepancy, which points to the invalidity of assuming potential flow. The

Table 2: Comparison between numerical and experimental values of hydrodynamic coefficients from the free decay tests

	Experiment (front)	Experiment (back)	RANS simulation (front)	RANS simulation (back)	Error (front) (%)	Error (back) (%)
$\omega_n$	2.215 rad/s	2.218 rad/s	2.221 rad/s	2.182 rad/s	0.29	1.61
$\zeta$	0.0395	0.0586	0.0400	0.0595	1.41	1.63
$I_{added}$	49.10 $kg.m^2$	48.92 $kg.m^2$	48.75 $kg.m^2$	50.87 $kg.m^2$	0.70	3.97
$C_{rad}$	10.34 Nm.s	15.32 Nm.s	10.45 Nm.s	15.82 Nm.s	1.1	3.3

response amplitude is overpredicted, most likely because the linear potential theory underestimates the damping coefficient and does not account for viscous effects leading to losses due to flow separation. In contrast, we compare in Figure 12 the flaps response as determined from RANS numerical simulation with the one measured in the wave tank for an incident wave having a period of 3 seconds and height of 0.08m. The plots show 1% and 2% differences in the steady state amplitudes of the responses of the front flap and back flap, respectively, which validates the performance of the RANS simulations in predicting the response amplitude.

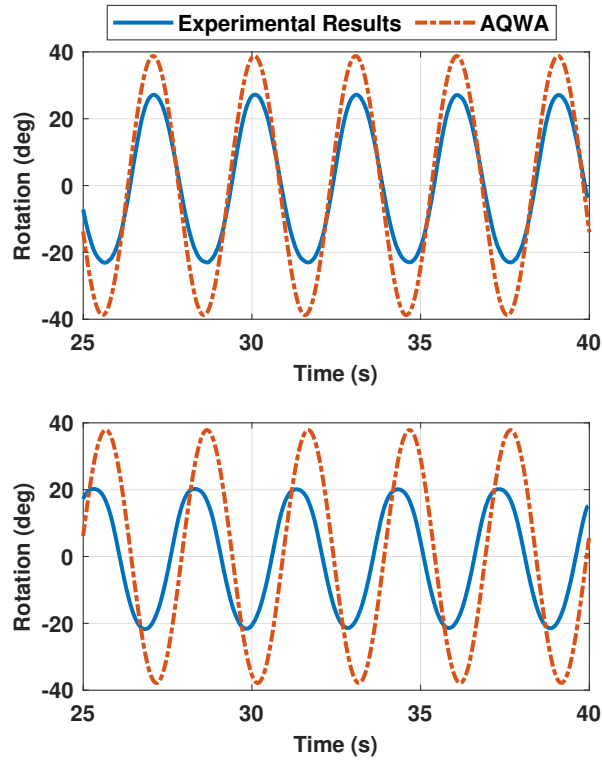


Figure 11: Comparison of the time series of the flaps response from AQWA with the experiments under regular wave excitation with a period of 3s and a height 0.08m for front flap (top) and back flap with added mechanical damping (bottom)

The RANS simulations as presented above were computationally expensive. For instance, each of the forced simulations, presented above, took 72 hours to compute 40 seconds of the response for the model. Evaluating the power matrix required about 125 simulations at the full scale, which in turn requires a larger mesh requirements in terms of size and number of points. To balance the computational cost and accuracy, we performed additional simulations using Euler’s equations with two different mesh sizes, fine mesh with 5.5M elements and coarse

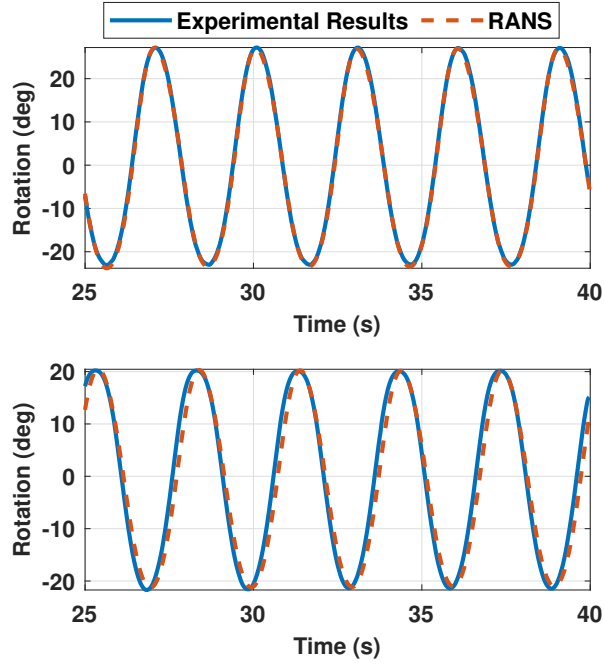


Figure 12: Comparison of the flaps response under regular wave excitation from the RANS simulations with experiments for waves with a period of 3s and a height 0.08m for front flap (top) and back flap with added mechanical damping (bottom)

mesh with 0.8M elements. Time series of the rotation angles of the front and back flaps from these simulations and those obtained from RANS simulation (fine mesh with 5.5M elements) and measured experimentally are compared in Figure 13. The accuracy of predicted values from all simulations is based on the percentage of error in the root-mean-square (RMS) values with respect to the measured RMS values. These errors along with the computational time required to simulate 40 seconds are presented in Table 3. All simulations were conducted on a workstation with Intel(R) Xeon(R) W-2155 16 cores processor and 64GB of RAM. The data signify that solving Euler's equation with a coarse mesh significantly reduces the computational time by 90% with an error of 11%, which is close to the acceptable 10% difference suggested by [56] as a threshold for validating numerical simulations. Furthermore, and although there is no theoretical foundation underpinning the acceptable level of prediction error of about 10%, we base it on how close the design is to achieve its stated goal. The conceptual design takes place at an early stage in the design process and based on expected performance of the different components. At later stages, the final design can be varied to recover 10% if needed to ensure that the F-OSWEC can generate 100 kW. If we allow for assuming a much larger acceptable error level, we may not be able to recover in the final design. This approach can be valuable in optimizing the design of the OSWEC and estimating its performance in the early stages of the design, where it is required to be estimated if a specific configuration meets a specific target. Therefore, it will be employed to conduct all simulations required to estimate the power matrix of the self-balanced dual-flap OSWEC.

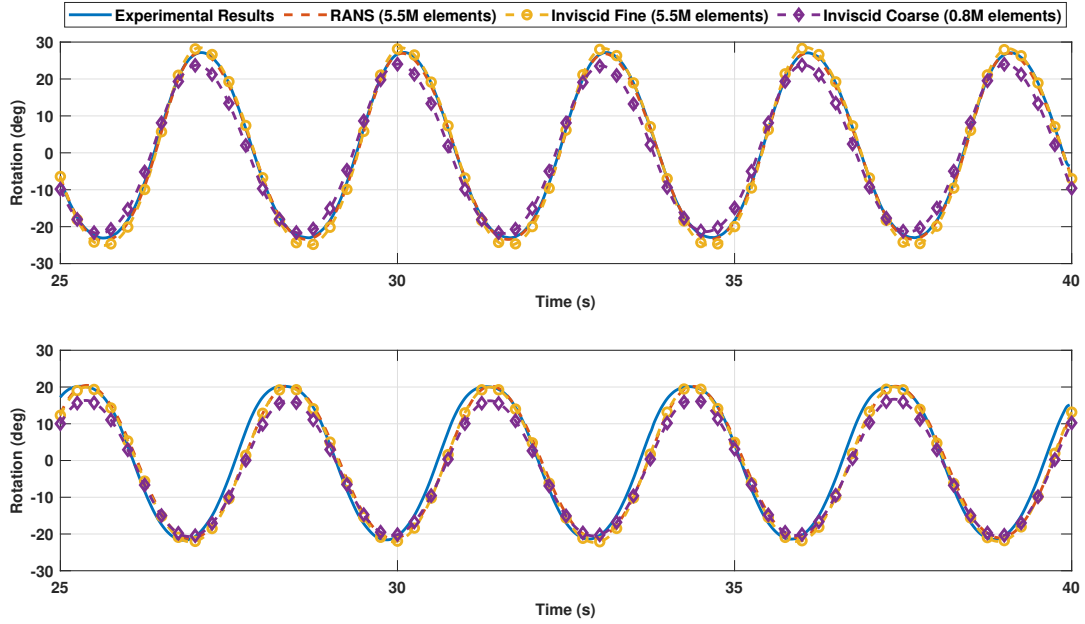


Figure 13: Comparison of simulated time series under regular wave forcing using a 3s wave period and 0.08m wave height obtained from different solvers and mesh resolutions for front (top) and back flaps (bottom)

Table 3: Required time to compute 40s of the response and corresponding error relative to measured value at 0.08m wave height and 3s wave period (near the natural frequency)

	Computational time	Error (front) (%)	Error (back) (%)
RANS	72 hrs.	1.03	1.68
Inviscid (fine mesh)	57 hrs.	6.84	0.99
Inviscid (coarse mesh)	7 hrs.	10.36	10.93
AQWA	0.3 hrs.	52.75	80.65

## 5. Power matrix and PTO loads for full-scale dual-flap OSWEC

In the full-scale simulations, the wave tank boundary conditions were changed to those of open water. Specifically, the side and bottom walls were set as symmetry boundary conditions to model zero-shear slip walls. The downstream boundary condition was set to be outflow boundary to extrapolate the flow velocity and pressure from the interior. The simulations solving unsteady Euler’s equation were conducted for the wave resources at the PacWave South site (Figure 1) to determine the expected annual energy production. In all numerical simulations, we used identical front and back flaps.

Figure 14 shows the estimated annual absorbed power by the two 12 m flaps based on wave conditions at the PacWave South site (Figure 1). Using these values and the percentage of occurrence of the waves, the estimated annual absorbed mechanical energy based on regular wave forcing without considering any losses is 4.63 GWh corresponding to an annual average power of 528 kW. Different sources of losses will affect that estimated power

in a significant way. The two major losses are due to the motion of the mooring platform supporting the flap and the PTO system. Based on wave tank experiments, it was assumed that losses due to the moving platform are about 30% [42]. Based on our experience and previously conducted dynamometer dry-tests using a passive mechanical motion rectifier (MMR), it is further assumed that the PTO efficiency distribution varies between 30% and 80% depending on wave period and height [13]. This efficiency increases as the wave period or the wave height is increased. The contour lines in Figure 15 show the assumed efficiency based on wave conditions. Furthermore, because the design is based on a rated power of 400 kW, the absorbed power is limited to this value. Considering all losses and rated power limit, the estimated electrical power matrix is presented in Figure 15. Using these values it is estimated that the annual generated energy, on the basis of regular waves, to be about 1.79 GWh corresponding to an annual average power of 205 kW. It is fair to expect that this estimate will be reduced to a value close to the targeted power of 100 kW when considering irregular wave forcing.

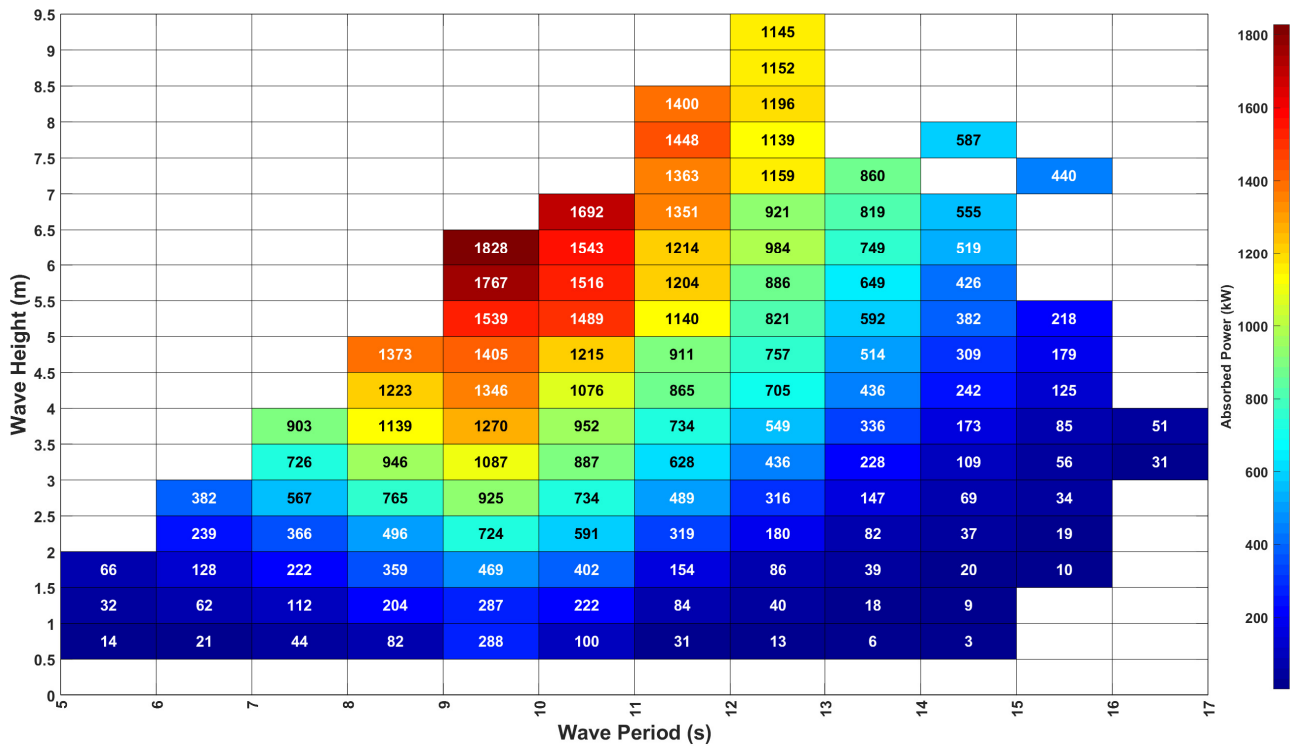


Figure 14: Estimate of absorbed power for different wave conditions defined in JPD

### 5.1. Capture width ratio

The Capture Width Ratio (CWR) is defined as the percentage of the absorbed power relative to the the wave power flowing through the WEC [10]. It is calculated by dividing the total absorbed power by the WEC over the product of the wave energy flux and the WEC width, i.e.

$$CWR = \frac{\text{Absorbed Power}}{\text{Wave Energy Flux} * \text{Width of Flap}} \quad (10)$$

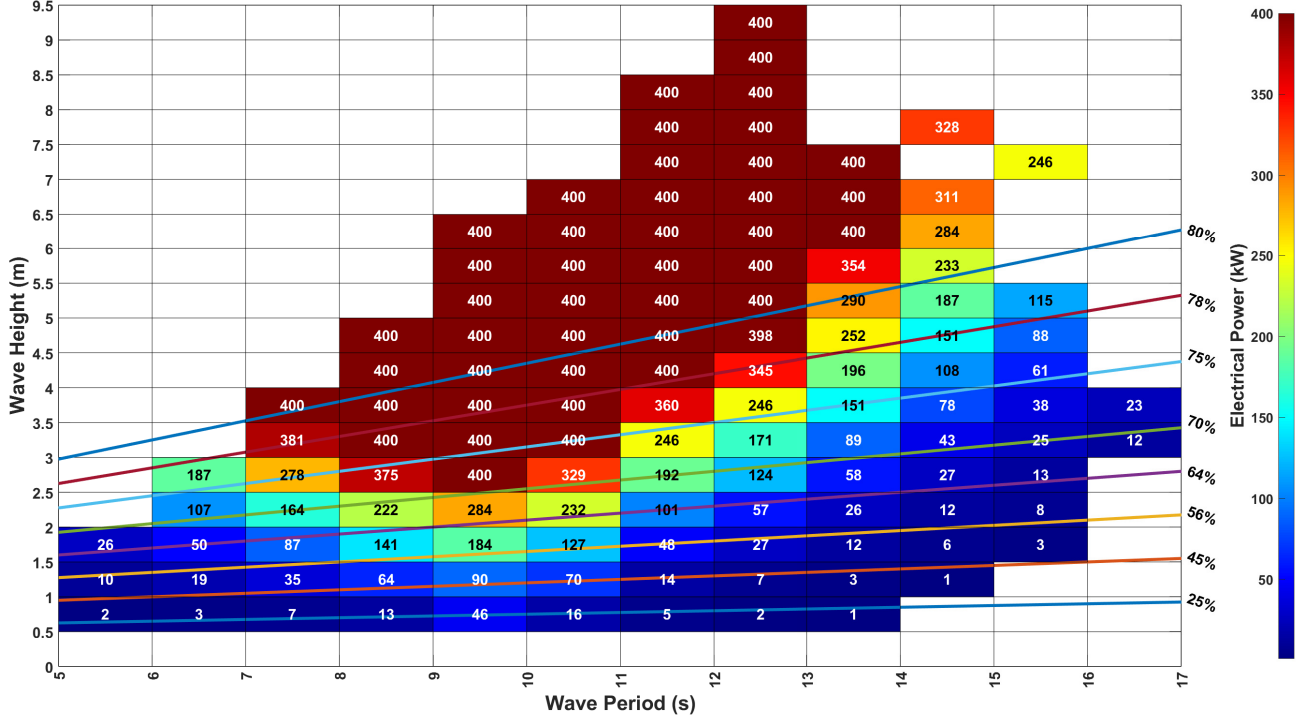


Figure 15: Power matrix based on a rated power of 400 kW and assumed PTO efficiency that varies between 30 and 80 % depending on wave period and height as shown by the contour levels

The wave energy flux is the wave power density per unit of wave-crest width. In deep water it is given by [57]:

$$P_w(\omega) = \frac{\rho g^2}{64\pi} H_{m0}^2 T_e \quad (11)$$

where  $\rho$  is the seawater density,  $g$  is the gravitational acceleration,  $H_{m0}$  is the significant wave height, and  $T_e$  is the energy period.

Applying equation 11 for the wave heights and periods in Figure 1 and multiplying it by the joint probability density as presented in the same figure, the total wave energy in an average year was determined to be 0.35 GWh/m. Using the yearly absorbed energy of 4.63 GWh by the 12-m wide flaps, the estimated CWR by the two flaps was determined to be 1.1. A CWR higher than one implies that the absorbed power is higher than the available one, which may seem unreasonable. However, considering that the waves can recover before reaching the second flap, it is reasonable to expect a CWR that is larger than 1.

## 5.2. PTO loads

Representing the hydrodynamic torque,  $T_{PTO}$ , by

$$T_{PTO} = C_{PTO} \dot{\theta} \quad (12)$$

where  $C_{PTO}$  is the PTO damping coefficient, the response of the flap under harmonic excitation is determined by applying Newton's second law, which yields

$$(I + I_a(\omega))\ddot{\theta} + C_r(\omega)\dot{\theta} + C_D(\omega)\dot{\theta}|\dot{\theta}| + C_{PTO}\dot{\theta} + k\theta = T_0\sin(\omega t + \phi) \quad (13)$$

where  $I$  is the mass moment of inertia of the flap,  $I_{added}$  is the added mass moment of inertia,  $C_r$  is the radiation damping coefficient,  $C_D$  is the viscous drag coefficient,  $k$  is the stiffness coefficient,  $\omega$  is the wave frequency, and  $T_0$  is the amplitude of the excitation torque. Under harmonic excitation, and assuming a response  $\theta = \theta_0\cos(\omega t)$ , a linearized version of equation 13 is obtained by using the first term of the Fourier expansion of the nonlinear drag term:

$$\sin(\omega t)|\sin(\omega t)| = \frac{8}{3\pi}\sin(\omega t) - \frac{8}{15\pi}\sin(3\omega t) - \frac{8}{105\pi}\sin(5\omega t) + \dots \quad (14)$$

Identification of the coefficients in equation 13 was performed using data from forced RANS simulations without waves or PTO. In the forced simulations, a harmonic torque with known amplitude was applied at the hinge of the flap. Under harmonic excitation, and based on the solution of the linearized equation, the amplitude of the applied torque  $T_0$ , response amplitude of rotation  $\theta_0$ , and phase difference  $\phi$ , are related by:

$$I_{added} = \frac{k}{\omega^2} - \frac{T_0\sin(\phi)}{\theta_0\omega^2} - I \quad (15)$$

$$\frac{8}{3\pi}C_D\omega\theta_0 + C_r = \frac{T_0\cos(\phi)}{\theta_0\omega} \quad (16)$$

Using these equations and data from the forced simulation, it was determined that  $C_r = 0.17$  MNm.s,  $C_D = 13.13$  MNm.s<sup>2</sup>, and  $I_{added} = 7.29 \times 10^3$  ton.m<sup>2</sup>.

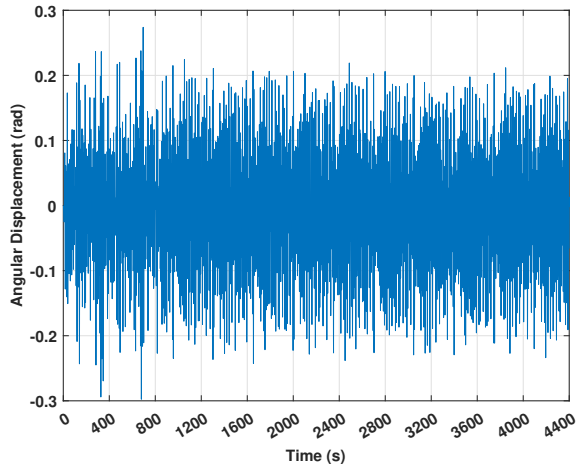
Through impedance matching, the optimal PTO damping,  $C_{PTO}|_{optimal}$ , is approximated as [58]

$$C_{PTO}|_{optimal} = \sqrt{\left(C_r + \frac{8}{3\pi}C_D\omega\theta_0\right)^2 + \left(\frac{k}{\omega} - \omega(I + I_{added})\right)^2} \quad (17)$$

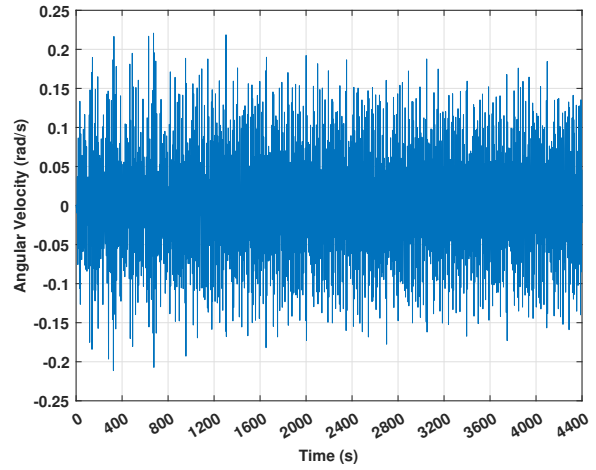
Under optimal conditions and for excitation near the natural frequency,  $C_{PTO}|_{optimal}$  was estimated to be 3.5 MNm.s. To account for the damping moment effect on the flap motion and its angular velocity, we included this PTO load in a simulation under sea state 4 irregular wave conditions with a significant wave height 1.75 m and peak wave period 9.5 seconds. Plots of the angular displacement, angular velocity, damping torque, and generated power are presented in Figure 16. The RMS of the angular displacement, angular velocity were determined to be 0.097 rad and 0.072 rad/s, the RMS of the torque is 0.25 MN.m. The peak to average ratio of the torque is 3.75, while the peak to average ratio of the power is 9.60. It is important to note here that a higher peak to average ratio may be realized if the numerical simulation is run over a longer duration or under higher sea state conditions.

## 6. Conclusions

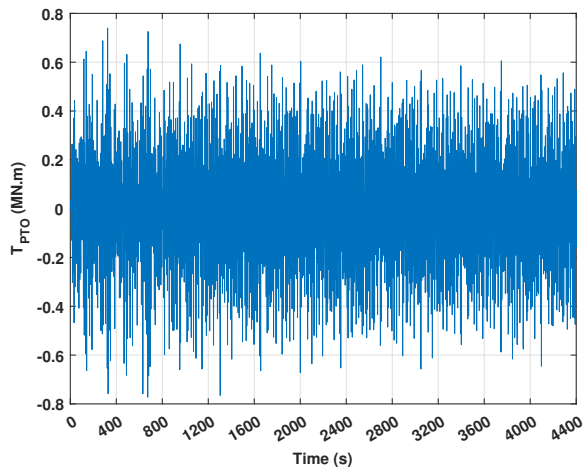
The hydrodynamic response of a self-balanced dual-flap OSWEC was simulated to predict its annual energy production, wave power capture and generated PTO loads when installed at the PacWave South site. To validate



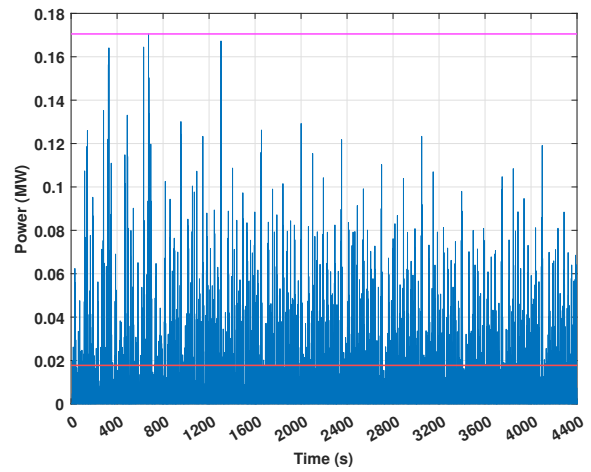
(a) Angular displacement in irregular waves



(b) Angular velocity in irregular waves



(c) PTO torque on a flap in irregular waves



(d) Mechanical power generated from PTO on a flap in irregular waves. Horizontal lines show peak and average values.

Figure 16: Flap performance under irregular wave conditions with peak wave period of 9.5 seconds and significant wave height of 1.75 m with PTO impeded

the simulation approach, experiments on a 1:10 scaled model were performed in the wave tank of Davidson Lab at Stevens Institute of Technology. Multi-fidelity simulations were performed to balance the computational cost and accuracy of predictions based on experimental tests. The results show that potential flow simulations overestimate the response by about 50% when the wave frequency is near the natural frequency of the WEC compared to the experimental results. Further simulations based on solving the RANS and Euler equations required a dynamic mesh to handle the complexity of the interaction between the flap and the incident waves. The comparison between the experimental and numerical results for the flaps rotation, natural frequency, added mass moment of inertia, damping ratio, and radiation damping coefficient shows better accuracy when using RANS simulations but also acceptable errors when solving Euler equations at a significantly reduced computational cost. Noting that prediction of the annual energy production requires hundreds of simulations, inviscid simulations using different spatial resolutions were performed and compared to the RANS simulations based on the realizable  $k-\epsilon$  model and experimental measurements. The results show that the computational cost can be significantly reduced (by 90%) while maintaining an acceptable percentage of accuracy (no more than 11% error) when using inviscid simulations with a relatively coarse mesh resolution when compared to using RANS simulations.

Extensive numerical simulations were then carried out to assess the expected annual energy production by a full-scale self-balanced dual-flap OSWEC, based on a specific design configuration for the PacWave South site taking into consideration all major losses. It is determined that the proposed WEC is able to generate 1.79 GWh (204 kW) annual electrical energy under regular wave excitation assuming an expected PTO efficiency that ranges from 30% to 80% and 0.88 GWh (100 kW) under irregular wave forcing. The CWR was determined to be 1.1, which reveals a significant improvement in energy capturing by a dual-flap OSWEC compared to single-flap OSWEC. All simulations were conducted with flaps being separated by half the wavelength (55m) of the most occurring wave (8.5s) at the PacWave South site.

It is important to note that a linear PTO was implemented in the equation of motion. Irregular wave forcing yielded an RMS of the input torque to the PTO of 0.25 MN.m with a peak to average ratio of 3.75, while the peak to average ratio of the power is 9.60. Further simulations having longer duration of irregular wave forcing may yield a higher peak-to-average ratio.

Finally, it is important to note that any developed framework such as the one proposed here will have its limitations depending on assumptions made. In this case, the performed simulations and experiments were limited to linear waves. As such the capability to predict response to extreme waves or nonlinear waves was not considered. The response under those conditions were considered in the final design as a part of the risk assessment and management processes. Variations in the design were implemented to reduce maximum internal stresses as required.

## **Acknowledgement**

This work was supported by the U.S. Department of Energy (DoE), Office of Energy Efficiency and Renewable Energy (EERE) under Award Number DE-EE0008953.

## References

- [1] A. LiVecchi, A. Copping, D. Jenne, A. Gorton, R. Preus, G. Gill, R. Robichaud, R. Green, S. Geerlofs, S. Gore, et al., Powering the blue economy; exploring opportunities for marine renewable energy in maritime markets, US Department of Energy, Office of Energy Efficiency and Renewable Energy. Washington, DC 207 (2019).
- [2] E. Gorr-Pozzi, J. Olmedo-González, R. Silva, Deployment of sustainable off-grid marine renewable energy systems in mexico, *Frontiers in Energy Research* 10 (2022) 1047167.
- [3] G. Giorgi, R. P. Gomes, J. C. Henriques, L. M. Gato, G. Bracco, G. Mattiazzo, Detecting parametric resonance in a floating oscillating water column device for wave energy conversion: Numerical simulations and validation with physical model tests, *Applied Energy* 276 (2020) 115421.
- [4] M. Masoomi, H. Sarlak, K. Rezanejad, Hydrodynamic performance analysis of a new hybrid wave energy converter system using openfoam, *Energy* 269 (2023) 126807.
- [5] B. N. Fox, R. P. Gomes, L. M. Gato, Analysis of oscillating-water-column wave energy converter configurations for integration into caisson breakwaters, *Applied Energy* 295 (2021) 117023.
- [6] A. Elhanafi, G. Macfarlane, A. Fleming, Z. Leong, Experimental and numerical investigations on the hydrodynamic performance of a floating–moored oscillating water column wave energy converter, *Applied energy* 205 (2017) 369–390.
- [7] M. Previsic, Offshore wave energy conversion devices, Electric Power Research Institute (EPRI) Report, Palo Alto (USA), 2004 (2004) 26–130.
- [8] L. Margheritini, D. Vicinanza, P. Frigaard, Ssg wave energy converter: Design, reliability and hydraulic performance of an innovative overtopping device, *Renewable Energy* 34 (2009) 1371–1380.
- [9] S. Parmeggiani, J. F. Chozas, A. Pecher, E. Friis-Madsen, H. Sørensen, J. P. Kofoed, Performance assessment of the wave dragon wave energy converter based on the equimar methodology, in: 9th ewtec 2011: Proceedings of the 9th European Wave and Tidal Conference, Southampton, UK, 5th-9th September 2011, University of Southampton, 2011.
- [10] A. Babarit, A database of capture width ratio of wave energy converters, *Renewable Energy* 80 (2015) 610–628.
- [11] B. Guo, J. V. Ringwood, Geometric optimisation of wave energy conversion devices: A survey, *Applied Energy* 297 (2021) 117100.
- [12] J. Mi, X. Wu, J. Capper, X. Li, A. Shalaby, R. Wang, S. Lin, M. Hajj, L. Zuo, Experimental investigation of a reverse osmosis desalination system directly powered by wave energy, *Applied Energy* 343 (2023) 121194.
- [13] X. Li, C. Chen, Q. Li, L. Xu, C. Liang, K. Ngo, R. G. Parker, L. Zuo, A compact mechanical power take-off for wave energy converters: Design, analysis, and test verification, *Applied Energy* 278 (2020) 115459.
- [14] M. Folley, T. Whittaker, M. Osterried, The oscillating wave surge converter, in: The Fourteenth International Offshore and Polar Engineering Conference, OnePetro, 2004.
- [15] T. Whittaker, D. Collier, M. Folley, M. Osterried, A. Henry, M. Crowley, The development of oyster—a shallow water surging wave energy converter, in: Proceedings of the 7th European wave and tidal energy

- conference, 2007, pp. 11–14.
- [16] M. Folley, T. Whittaker, J. Van't Hoff, The design of small seabed-mounted bottom-hinged wave energy converters, in: Proceedings of the 7th European wave and tidal energy conference, volume 455, Citeseer, 2007, p. 312.
- [17] M. Choiniere, J. Davis, N. Nguyen, N. Tom, M. Fowler, K. Thiagarajan, Hydrodynamics and load shedding behavior of a variable-geometry oscillating surge wave energy converter (oswec), *Renewable Energy* (2022).
- [18] M. Folley, T. Whittaker, A. Henry, The effect of water depth on the performance of a small surging wave energy converter, *Ocean Engineering* 34 (2007) 1265–1274.
- [19] Y.-H. Yu, D. Jenne, R. Thresher, A. Copping, S. Geerlofs, L. Hanna, Reference model 5 (rm5): Oscillating surge wave energy converter, Technical Report, National Renewable Energy Lab.(NREL), Golden, CO (United States), 2015.
- [20] A. Pecher, J. P. Kofoed, J. Espedal, S. Hagberg, Results of an experimental study of the langlee wave energy converter, in: The Twentieth International Offshore and Polar Engineering Conference, OnePetro, 2010.
- [21] R. P. Gomes, L. M. Gato, J. C. Henriques, J. C. Portillo, B. D. Howey, K. M. Collins, M. R. Hann, D. M. Greaves, Compact floating wave energy converters arrays: Mooring loads and survivability through scale physical modelling, *Applied Energy* 280 (2020) 115982.
- [22] A. Babarit, J. Hals, M. J. Muliawan, A. Kurniawan, T. Moan, J. Krokstad, Numerical benchmarking study of a selection of wave energy converters, *Renewable energy* 41 (2012) 44–63.
- [23] E. Rusu, F. Onea, Estimation of the wave energy conversion efficiency in the atlantic ocean close to the european islands, *Renewable Energy* 85 (2016) 687–703.
- [24] L. Rusu, F. Onea, The performance of some state-of-the-art wave energy converters in locations with the worldwide highest wave power, *Renewable and Sustainable Energy Reviews* 75 (2017) 1348–1362.
- [25] N. Guillou, G. Chapalain, Annual and seasonal variabilities in the performances of wave energy converters, *Energy* 165 (2018) 812–823.
- [26] G. Giannini, P. Rosa-Santos, V. Ramos, F. Taveira-Pinto, Wave energy converters design combining hydrodynamic performance and structural assessment, *Energy* 249 (2022) 123641.
- [27] M. Kelly, N. Tom, Y.-H. Yu, A. Wright, M. Lawson, Annual performance of the second-generation variable-geometry oscillating surge wave energy converter, *Renewable Energy* 177 (2021) 242–258.
- [28] C. Ni, W. Peng, An integrated approach using empirical wavelet transform and a convolutional neural network for wave power prediction, *Ocean Engineering* 276 (2023) 114231.
- [29] A. Rahimi, S. Rezaei, J. Parvizian, S. Mansourzadeh, J. Lund, R. Hssini, A. Düster, Numerical and experimental study of the hydrodynamic coefficients and power absorption of a two-body point absorber wave energy converter, *Renewable Energy* 201 (2022) 181–193.
- [30] A. G. Majidi, B. Bingölbali, A. Akpınar, E. Rusu, Wave power performance of wave energy converters at high-energy areas of a semi-enclosed sea, *Energy* 220 (2021) 119705.
- [31] R. Carballo, N. Arean, M. Álvarez, I. López, A. Castro, M. López, G. Iglesias, Wave farm planning through high-resolution resource and performance characterization, *Renewable Energy* 135 (2019) 1097–1107.

- [32] S. Astariz, G. Iglesias, The economics of wave energy: A review, *Renewable and Sustainable Energy Reviews* 45 (2015) 397–408.
- [33] K. Ruehl, D. D. Forbush, Y.-H. Yu, N. Tom, Experimental and numerical comparisons of a dual-flap floating oscillating surge wave energy converter in regular waves, *Ocean Engineering* 196 (2020) 106575.
- [34] M. A. Bhinder, A. Babarit, L. Gentaz, P. Ferrant, Potential time domain model with viscous correction and cfd analysis of a generic surging floating wave energy converter, *International Journal of Marine Energy* 10 (2015) 70–96.
- [35] C.-C. Lin, Y.-C. Chow, S.-Y. Tzang, The viscous effect in power capture of bottom-hinged oscillating wave surge converters, in: *Proceedings of the 4rd Asian Wave and Tidal Energy Conference (AWTEC)*, Taipei, Taiwan, 2018, pp. 423–1.
- [36] Y. Wei, A. Rafiee, A. Henry, F. Dias, Wave interaction with an oscillating wave surge converter, part i: Viscous effects, *Ocean Engineering* 104 (2015) 185–203.
- [37] P. Schmitt, B. Elsaesser, On the use of openfoam to model oscillating wave surge converters, *Ocean Engineering* 108 (2015) 98–104.
- [38] M. Bhinder, C. Mingham, D. Causon, M. Rahmati, G. Aggidis, R. Chaplin, Numerical modelling of a surging point absorber wave energy converter, in: *Proc. of 8th European Wave and Tidal Energy Conference EWTEC*, 2009.
- [39] A. R. Dallman, V. S. Neary, Characterization of us wave energy converter (wec) test sites: A catalogue of met-ocean data (part 2), Sandia National Laboratories, Albuquerque, NM (2014).
- [40] A. Ahmed, J. Mi, J. Haung, M. R. Hajj, R. Datla, L. Zuo, Multi-fidelity modeling and simulation of dual-flap oscillating surge wave energy converter, in: *OCEANS 2023 - MTS/IEEE U.S. Gulf Coast*, 2023, pp. 1–6.
- [41] Q. Li, J. Mi, X. Li, S. Chen, B. Jiang, L. Zuo, A self-floating oscillating surge wave energy converter, *Energy* 230 (2021) 120668.
- [42] J. Mi, J. Huang, X. Li, L. Yang, A. Ahmed, R. Datla, M. Folly, M. Hajj, L. Zuo, Dual-flap floating oscillating surge wave energy converter: Modelling and experiment evaluation, *IFAC-PapersOnLine* 55 (2022) 138–143.
- [43] M. Lawson, B. B. Garzon, F. Wendt, Y.-H. Yu, C. Michelen, Coer hydrodynamic modeling competition: Modeling the dynamic response of a floating body using the wec-sim and fast simulation tools, in: *International Conference on Offshore Mechanics and Arctic Engineering*, volume 56574, American Society of Mechanical Engineers, 2015, p. V009T09A005.
- [44] Y. Wang, L. Wang, Towards realistically predicting the power outputs of wave energy converters: Nonlinear simulation, *Energy* 144 (2018) 120–128.
- [45] G. Dunkle, B. Robertson, G. García-Medina, Z. Yang, *Pacwave wave resource assessment* (2020).
- [46] G. Payne, Guidance for the experimental tank testing of wave energy converters, *SuperGen Marine* 254 (2008) 1–51.
- [47] H. C. Chen, V. C. Patel, S. Ju, Solutions of reynolds-averaged navier-stokes equations for three-dimensional incompressible flows, *Journal of Computational Physics* 88 (1990) 305–336.
- [48] J.-P. Bourguignon, H. Brezis, Remarks on the euler equation, *Journal of functional analysis* 15 (1974)

341–363.

- [49] C. W. Hirt, B. D. Nichols, Volume of fluid (vof) method for the dynamics of free boundaries, *Journal of computational physics* 39 (1981) 201–225.
- [50] S. Mathur, J. Murthy, A pressure-based method for unstructured meshes, *Numerical heat transfer* 31 (1997) 195–215.
- [51] B. A. Nichita, I. Zun, J. R. Thome, A level set method coupled with a volume of fluid method for modeling of gas-liquid interface in bubbly flow, *Journal of fluids engineering* 132 (2010).
- [52] J. Newman, *Marine hydrodynamics 40th anniversary edition*, 2017.
- [53] Z. Wu, H. Zhang, Z. Liu, G. Tian, X. Hou, F. Yang, Force and energy analysis of single-piston free-piston expander—linear generator, *Energy* 251 (2022) 123926.
- [54] D. Snyder, E. Koutsavdis, J. Anttonen, Transonic store separation using unstructured cfd with dynamic meshing, in: *33rd AIAA fluid dynamics conference and exhibit*, 2003, p. 3919.
- [55] I. Kimura, T. Hosoda, A non-linear  $k-\epsilon$  model with realizability for prediction of flows around bluff bodies, *International Journal for Numerical Methods in Fluids* 42 (2003) 813–837.
- [56] C. Windt, J. Davidson, J. V. Ringwood, High-fidelity numerical modelling of ocean wave energy systems: A review of computational fluid dynamics-based numerical wave tanks, *Renewable and Sustainable Energy Reviews* 93 (2018) 610–630.
- [57] X. Hu, Y. Fang, Y. Wu, H. Wu, H.-S. Kang, An approach to assess the potential of wave energy resources based on directional energy flux, *Ocean Engineering* 287 (2023) 115732.
- [58] Y. Cheng, C. Ji, G. Zhai, Fully nonlinear analysis incorporating viscous effects for hydrodynamics of an oscillating wave surge converter with nonlinear power take-off system, *Energy* 179 (2019) 1067–1081.